Ablation behavior and mechanisms of ZrC−SiC−MoSi₂ coated C/C−SiC−ZrC ceramic matrix composites under oxyacetylene torch

Meng-meng SHAO, Zhao-ke CHEN, Xin-shuang WANG, Qing-bo WEN, Xiang XIONG

State Key Laboratory of Powder Metallurgy, Central South University, Changsha 410083, China

Abstract: To further improve the anti-ablation property of C/C composites in different ablation environments, ZrC−SiC−MoSi₂ coatings containing 34 wt.% and 60 wt.% Zr were prepared on C/C−SiC−ZrC ceramic matrix composites via slurry painting (SP) method. And the ablation behavior of the coated composites was investigated in oxyacetylene torch environment with three kinds of fluxes of oxygen and acetylene. The results show that with the increase of Zr content, the particle sizes of ZrC and SiC in the coatings are significantly reduced, with the particles distributing more homogeneously. The linear ablation rates of the coatings with 60 wt.% Zr increase with the increase of oxygen and acetylene fluxes, while for the coatings with 34 wt.% Zr, the linear ablation rates increase at the beginning and then decrease. The ablation mechanisms of the coatings under different conditions were discussed as well. With the increase of oxygen and acetylene fluxes, main ablation mechanisms change from oxidation to oxidation plus evaporation and then to the combination of oxidation, evaporation and denudation.

Key words: C/C−SiC−ZrC composite; ZrC−SiC−MoSi₂ coating; slurry; ablation

1 Introduction

Carbon/carbon composites (C/Cs) are considered as the most promising candidates for ultrahigh temperature structural applications in aircraft and aerospace fields, because of the combined advantages of high strength, high thermal stability, low density, as well as low coefficient of thermal expansion (CTE) [1]. However, C/Cs are easy to be oxidized at temperatures over 400 °C, which strongly limits their high-temperature applications in oxygen-containing environment [2]. Thus, oxidation sensitivity of C/Cs is a key problem to be solved for the purpose of application in a high-temperature aerobic environment [3].

Introducing ultra-high temperature ceramics (UHTCs) into C/Cs is an effective method to improve their ablation performance [4]. Among the UHTCs, ZrC is one of the most widely used

materials. However, ZrC cannot be used alone because the formed ZrO₂ is usually loose, which is detrimental to the ablation performance of C/Cs [5]. As the oxide of SiC, SiO₂ has excellent self-healing capability which could effectively fill the porous ZrO₂ skeleton to form a dense and continues ZrO₂−SiO₂ phase [6,7]. Moreover, C/C−SiC−ZrC is widely used as thermal structural materials [8] and heat-protection material with improved ablation resistance [9]. Even though the oxidation resistance of the C/C−SiC−ZrC composites has been dramatically improved via the introduction of SiC and ZrC phases, bare carbon fibers are still inevitable. The bare carbon fibers on the surface of the composites can be severely oxidized in ablation environment, resulting in the decrease of ablation performance. Accordingly, protective UHTC coatings on the surface of the C/C−SiC−ZrC composites are highly demanded.

Pack cementation (PC) [10], chemical vapor

deposition (CVD) [11], plasma spray (PS) [12], and slurry painting (SP) [13] are main methods to prepare UHTC coatings. Among these methods, SP should be a promising method for preparing UHTC coatings on the C/C−SiC−ZrC composites. For example, ZHANG et al [14] prepared a bilayer coating with a HfB_2−$MoSi_2$ outer layer fabricated by SP method on C/Cs composites, which possesses excellent oxidation resistance. QIAN et al [15] reported a Y_2O_3-doped mullite−$ZrSiO_4$ coating prepared by SP, which exhibits good corrosion resistance.

In the past decades, much attention has been paid to the composition, structure design and preparation method of anti-ablation coatings as well as to their ablation behavior in a single ablation environment [16−18]. However, the ablation behavior and mechanism of UHTC coatings in different ablation environments is seldom explored. In fact, the application environment of thermal structural components in aerospace is rather complicated. Therefore, investigating the ablation behavior of thermal structural components in different gas flux environments is of key importance for their practical applications [19].

In this work, ZrC−SiC−$MoSi_2$ ceramic coatings with two different Zr contents were prepared on the C/C−SiC−ZrC substrates by slurry painting (SP) technology. In order to improve the density of the ceramic coatings and the bonding strength with the substrate, Al_2O_3 and CeO_2 were used as sintering aids. The microstructure and phase composition of the as-prepared coatings were characterized using SEM and XRD, respectively. The ablation behavior of the ZrC−SiC−$MoSi_2$ ceramic coatings was tested by oxyacetylene flame with three fluxes of oxygen and acetylene. The corresponding ablation mechanisms were discussed as well.

2 Experimental

2.1 Materials

The C/C−SiC−ZrC substrates, with the dimension of $d28$ mm × 10 mm, were cut from a bulk composite with a density of 2.05 g/cm³. After being polished with 1000 grit SiC paper, the substrates were cleaned by ethanol and then dried at 100 °C for 3 h. High purity powders were mixed together according to the following compositions

(mass fraction): (1) 34%Zr−51%Si−10%$MoSi_2$−5%(Al_2O_3+CeO_2) (denoted as ZSM-L) and (2) 60%Zr−25%Si−10%$MoSi_2$−5%(Al_2O_3+CeO_2) (denoted as ZSM-H). Zr and Si were the main compositions of the coatings. $MoSi_2$ was used as sintering aid to improve the density of the coating owing to its good wettability with ZrC and SiC. In addition, Al_2O_3 and CeO_2 were used as sintering aids to improve the liquid phase sintering of the coatings [4].

The mixed powders were ball milled for 20 h. Then, they were added into a polyvinyl alcohol (PVA) solution with powders/PVA mass ration of 3:1 to obtain the slurry. Subsequently, the slurry was brushed directly onto the C/C−SiC−ZrC substrate. After drying at 100 °C for 2 h, the brushed samples were placed in an electric furnace and sintered at 1900 °C in argon atmosphere for 4 h with a heating rate of 10 °C/min.

2.2 Ablation test

The anti-ablative properties of the ZrC−SiC−$MoSi_2$ coated C/C−SiC−ZrC samples were tested by an oxyacetylene torch. The distance between the gun tip and the ablated surface was 10 mm. The inner diameter of the gun tip was 2 mm, and the ablation angle was 90°. The samples were exposed to the flame for 60 s. The temperature of the oxyacetylene flame was measured using an optic pyrometer, and the maximal temperature was 2500−3000 °C. The linear ablation rate (R_l) was calculated according to Eq. (1):

$$R_l=\Delta l/t=(l_1-l_2)/t \tag{1}$$

where Δl (mm) is the thickness change before (l_1) and after (l_2) ablation, and t is the ablation time (s). In this work, three ablation conditions with different oxygen and acetylene fluxes were used to obtain different heat flux environments (Table 1). The ablative properties of the coatings in three ablation conditions were investigated.

Table 1 Oxygen and acetylene fluxes of three ablation conditions in ablation test

Condition No.	Gas flux/(L·s⁻¹)	
	Oxygen	Acetylene
1	1.1000	0.2627
2	1.5120	1.1160
3	2.0000	1.1160

2.3 Characterization

Phase compositions of the coatings before and after ablation were characterized by X-ray diffraction (XRD, D8 Advance, Brook, Germany). Microstructures of the coatings before and after ablation were analyzed by scanning electron microscopy (SEM, Quanta 250 FEG, FEI Ltd, CZ) equipped with energy dispersive X-ray spectroscopy (EDX, Elect plus, EDAX Inc, USA).

3 Results and discussion

3.1 Phase composition of coatings

XRD patterns of the as-prepared ZSM coatings are shown in Fig. 1. Both ZMS-L and ZMS-H coatings consist of ZrC, SiC, and $MoSi_2$ phases.

3.2 Microstructure of coatings

Figure 2 shows the SEM images of ZSM-L (Figs. 2(a, b)) and ZSM-H (Figs. 2(c, d)) coatings. The coating surface is dense and intact, in which $MoSi_2$ is distributed continuously around ZrC grains and fills the voids among ZrC grains effectively. Moreover, the good ductility and wettability of $MoSi_2$ with ZrC promotes the densification of
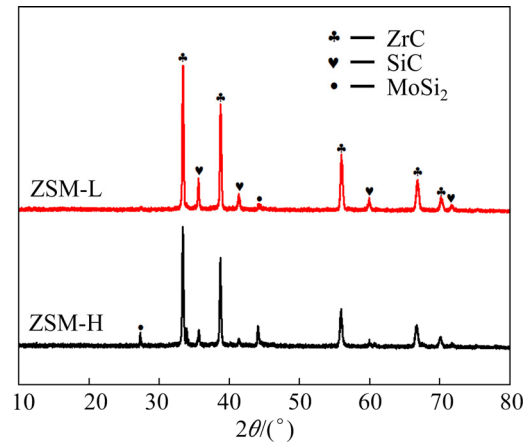

Fig. 1 XRD patterns of as-prepared ZSM coatings

$ZrC-SiC-MoSi_2$ coatings. Al_2O_3 can promote solid reaction [16] and prevent coating from cracking [20] by combining with SiC to inhibit microcracks expansion [21]. CeO_2 has high chemical activity, which is often used as surfactant. Moreover, $Al_2O_3-CeO_2$ has good wettability to SiC, which is beneficial to the densification of the coating [22]. In conclusion, the combination of Al_2O_3 and CeO_2 is able to increase the driving force for sintering and well promote the density of the coating. As a result,
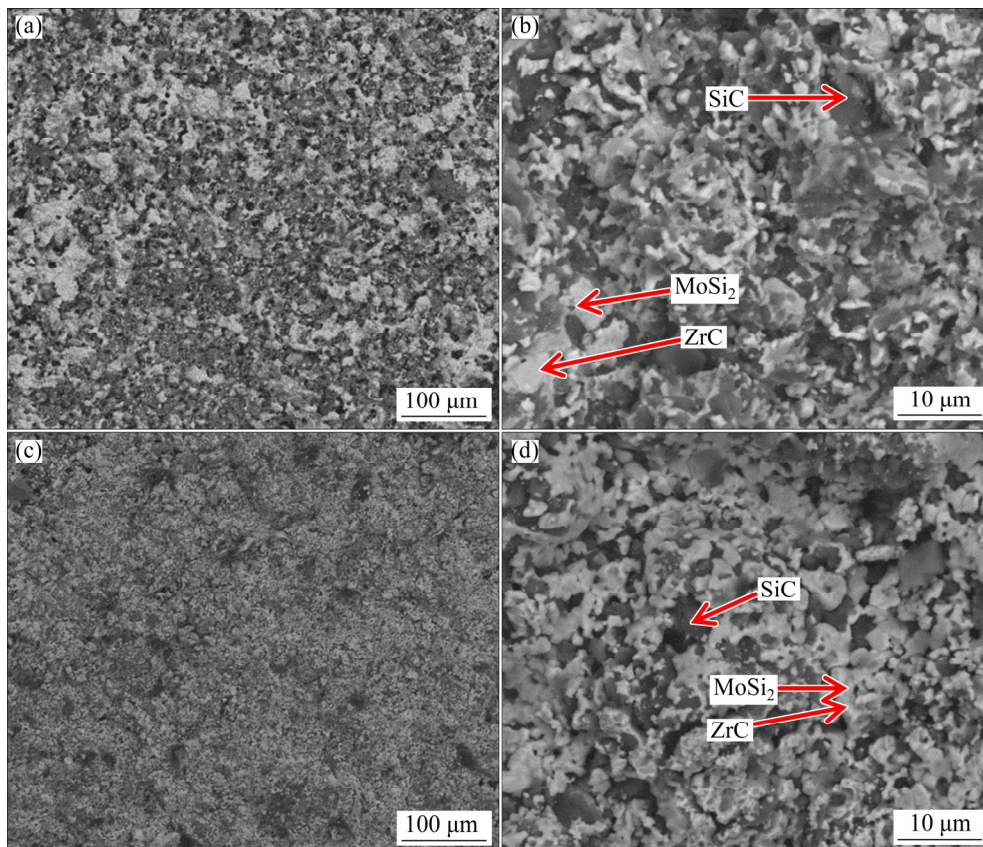

**Fig. 2** SEM images of ZSM-L (a, b) and ZSM-H (c, d) samples

the distribution of SiC and ZrC−MoSi$_2$ phases is homogeneous under the combined action of MoSi$_2$, Al$_2$O$_3$ and CeO$_2$. In addition, compared with the ZSM-L coating, the particle sizes of ZrC and SiC within the ZSM-H coating are smaller, and the particles are distributed more homogeneously. In conclusion, Zr content plays an important role in the surface morphology and microstructure of the coatings.

3.3 Anti-ablation property of coating

The linear ablation rates of the ZSM-H and ZSM-L coated samples are shown in Fig. 3. With the increase of heat fluxes, the linear ablation rates of ZSM-H samples increase gradually, while those of ZSM-L samples increase firstly, and then decrease. In comparison, the linear ablation rates of ZSM-H samples are lower than those of ZSM-L samples under Conditions 1 and 2. Especially under Condition 1, the linear ablation rate of ZSM-H samples is zero, showing a non-ablation characteristic. However, under Condition 3, the linear ablation rate of ZSM-H samples (1.86×10^{-2} mm/s) is higher than that of ZSM-L samples (4.4×10^{-3} mm/s). This is mainly attributed

to low adhesion of the oxides of ZSM-H samples, which are easy to be peeled off under high speed air-flow. However, the decrease of linear ablation rates of ZSM-L samples is mainly attributed to the volume expansion caused by SiO$_2$ phase. In conclusion, Zr content in the coating has a great influence on the ablation performance.

Figure 4 shows the photographs of the ZSM-H and ZSM-L coatings after ablation under three conditions. Three areas, namely central (A),
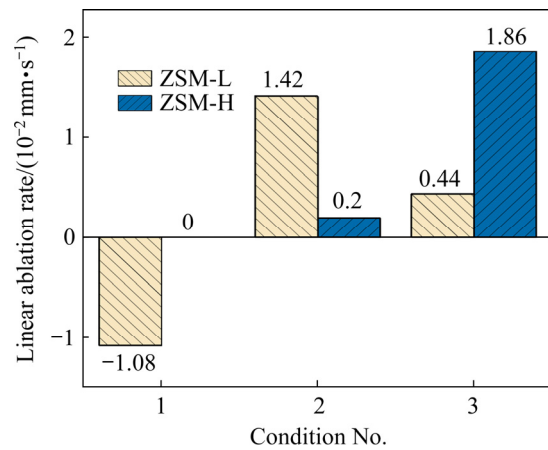
**Fig. 3** Linear ablation rates of ZSM-H and ZSM-L samples in three conditions
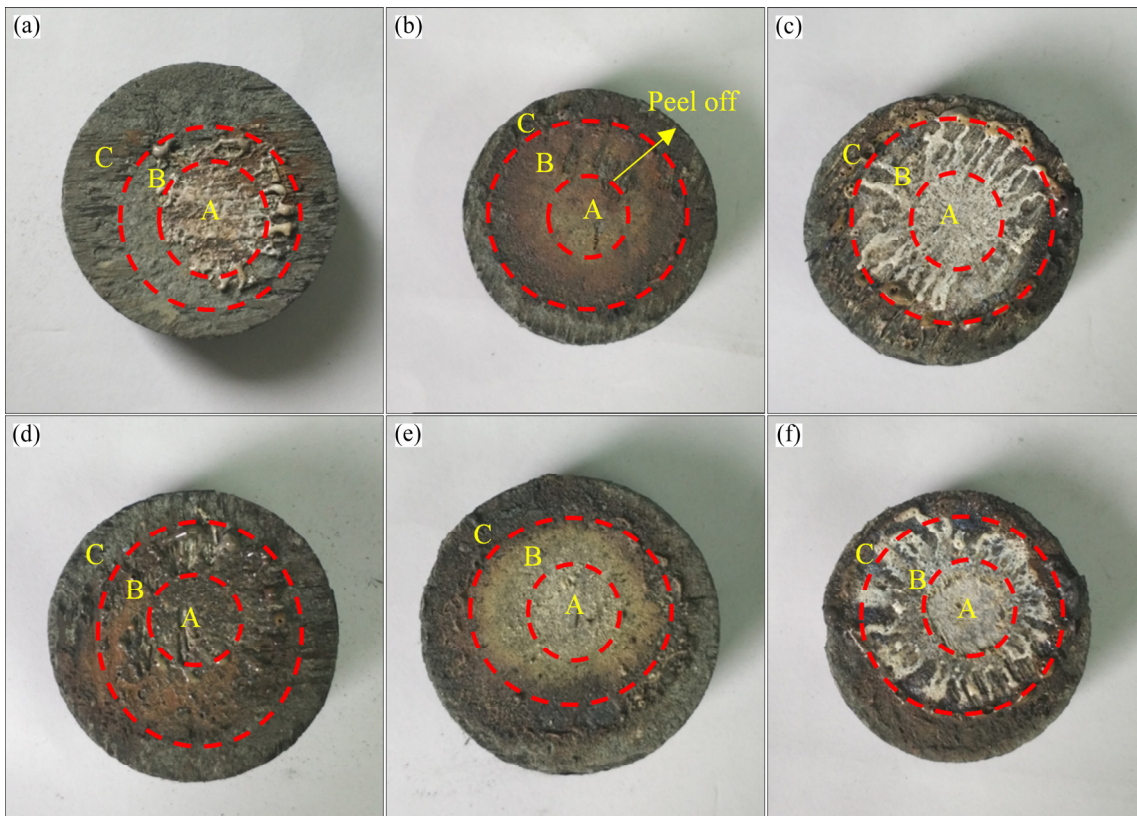
Fig. 4 Photographs of samples after ablation for 60 s: (a) ZSM-L, Condition 1; (b) ZSM-L, Condition 2; (c) ZSM-L, Condition 3; (d) ZSM-H, Condition 1; (e) ZSM-H, Condition 2; (f) ZSM-H, Condition 3

transition (B) and boundary (C) can be clearly identified on the surface of the samples. The central area of the samples suffers the severest mechanical erosion and the highest temperature [9].

According to the photographs of ZSM-L samples after ablation (Figs. 4(a−c)), a dense oxide layer is formed in the central area under Condition 1, which becomes loose with slight spallation under Condition 2. Under Condition 3, a white oxide scale in the shape of chrysanthemum is formed on the surface, which is due to the flowing of the liquid phase from the central area to the boundary area under high-speed air-flow. Regarding the ZSM-H samples, a dense and compact oxide layer is formed after ablation under Condition 1 (Fig. 4(d)), and a visible change in colors under Condition 2 (Fig. 4(e)). Under Condition 3 (Fig. 4(f)), an obvious ablation pit appears in the center of the chrysanthemum-shaped oxide layer, resulting in a higher linear ablation rate. The large difference of microstructure in the central, transition and boundary regions can be attributed to the variation of diameter of the oxyacetylene flame with the samples.

Figure 5 displays the XRD patterns obtained in the central area of ZSM-L and ZSM-H samples after ablation under three conditions. The surface of the samples after ablation is composed of monoclinic ZrO_2 (m-ZrO_2) and $ZrSiO_4$ (formed via the reaction between ZrO_2 and SiO_2). After ablation, amorphous SiO_2 is formed, which cannot be detected by XRD due to its amorphous nature. The intensity of m-ZrO_2 and $ZrSiO_4$ shows the highest value under Condition 2, indicating the best crystalline of the oxidation products. Moreover,
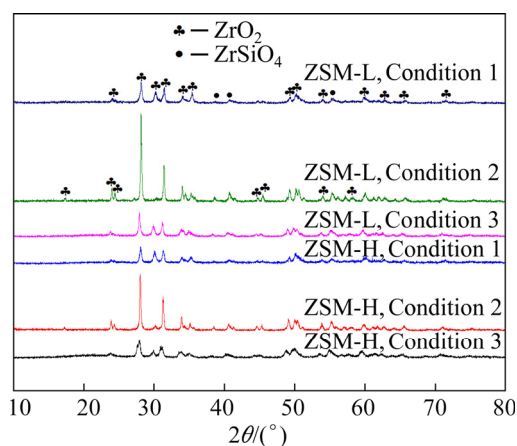
**Fig. 5** XRD patterns of ZSM-L and ZSM-H samples after ablation in three conditions

carbon peak is not observed, suggesting that the substrates are well protected.

Figures 6(a−d) show the surface morphologies and EDX analysis results of the ZSM-L samples after ablation under Condition 1. In the central area, a typical structure with ZrO_2 particles (Spot 2) embedded in glassy SiO_2 phase (Spot 1) is formed. In this structure, voids created by the release of volatile gas can be filled by the glass phase, resulting in a compact coating surface. In the transition area, the smooth coating comprises white spherical ZrO_2 particles, dark grey SiO_2, and faint grey $ZrSiO_4$ molten phase (Spot 3), forming a glass−ceramic skeleton structure [23]. The molten $ZrSiO_4$ phase, with a melting point of 1540 °C, can also fill in the ZrO_2 skeleton and form a dense ZrO_2−$ZrSiO_4$ double-phase layer [24]. In this case, $ZrSiO_4$ can seal defects (micro-holes and cracks) [25] and improve the stability of the SiO_2 glass layer [26].

Under Condition 2 (Figs. 6(e−h)), large ZrO_2 grains are formed after ablation, with micro-cracks and pores also appearing in the central area. The formation of micro-cracks is ascribed to the volume shrinkage of ZrO_2 phase during transformation from tetragonal (t-ZrO_2) to monoclinic ZrO_2 (m-ZrO_2). The pores are induced by the escape of gas products (SiO_2, SiO, CO_2, CO and MoO_3). In the transition area, the number of pores and cracks reduces.

Under Condition 3 (Figs. 6(i−l)), a loose coating surface is formed, with many holes and gullies observed in the central region. The loose surface is mainly composed of ZrO_2 scale, which is derived from the evaporation of liquid SiO_2 in the highest heat flux. The ZrO_2 scale can provide channels for the diffusion of oxygen and accelerate the oxidation of the substrate. In the transition area, bigger ZrO_2 particles are associated with fewer SiO_2 phase forming a SiO_2 depletion layer.

Surface morphologies of the ZSM-H sample after ablation under three conditions are shown in Fig. 7. Under Condition 1 (Figs. 7(a−d)), the coating in central area comprises decided bulges, which are caused by the scour of oxyacetylene flame. From the enlarged images, the bulges consist of fine ZrO_2 grains and glassy SiO_2 phase, in which the ZrO_2 grains are distributed in the glassy SiO_2 homogeneously. The existence of dispersed ZrO_2 particles can improve the surface viscosity and well weaken the depletion of SiO_2 phase. In transition
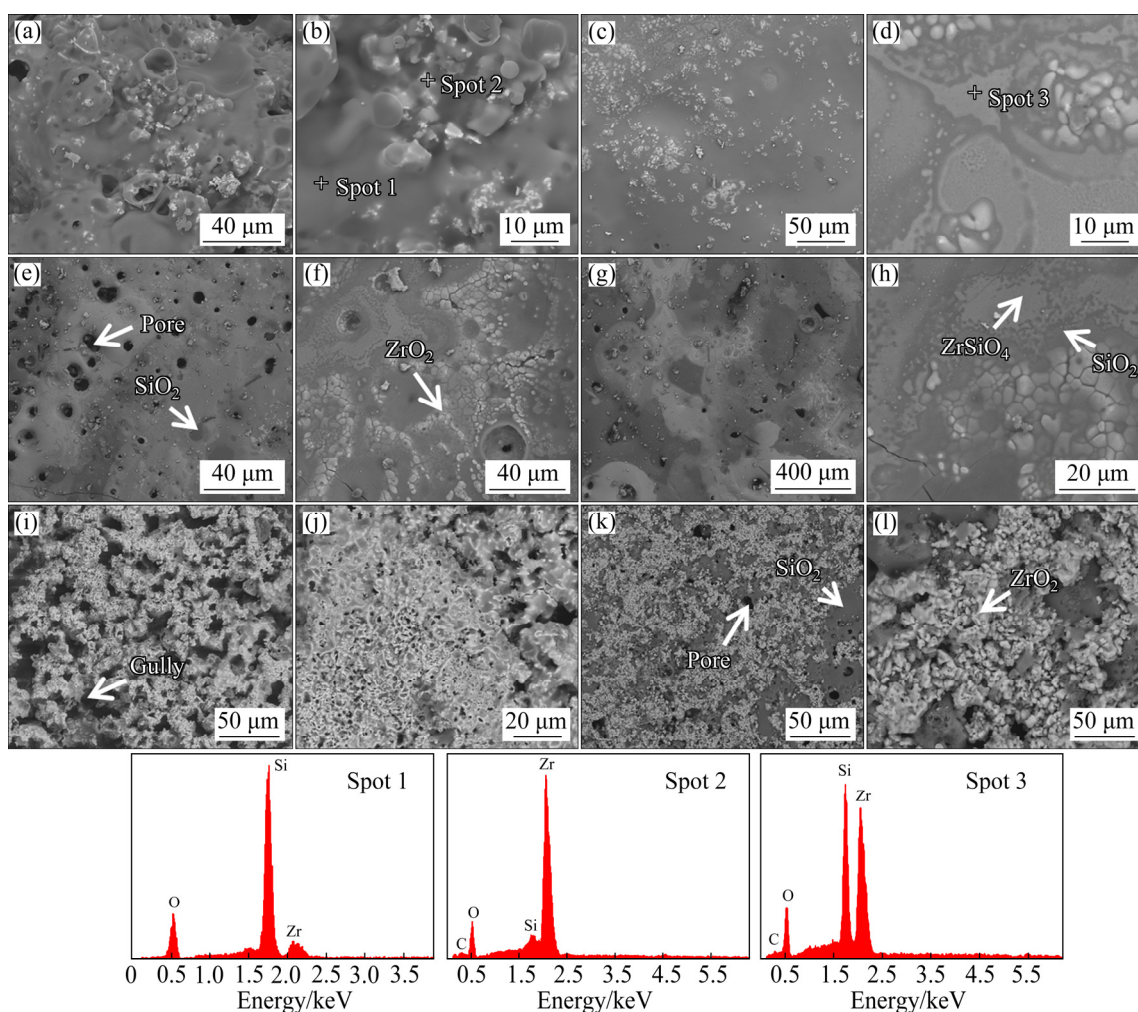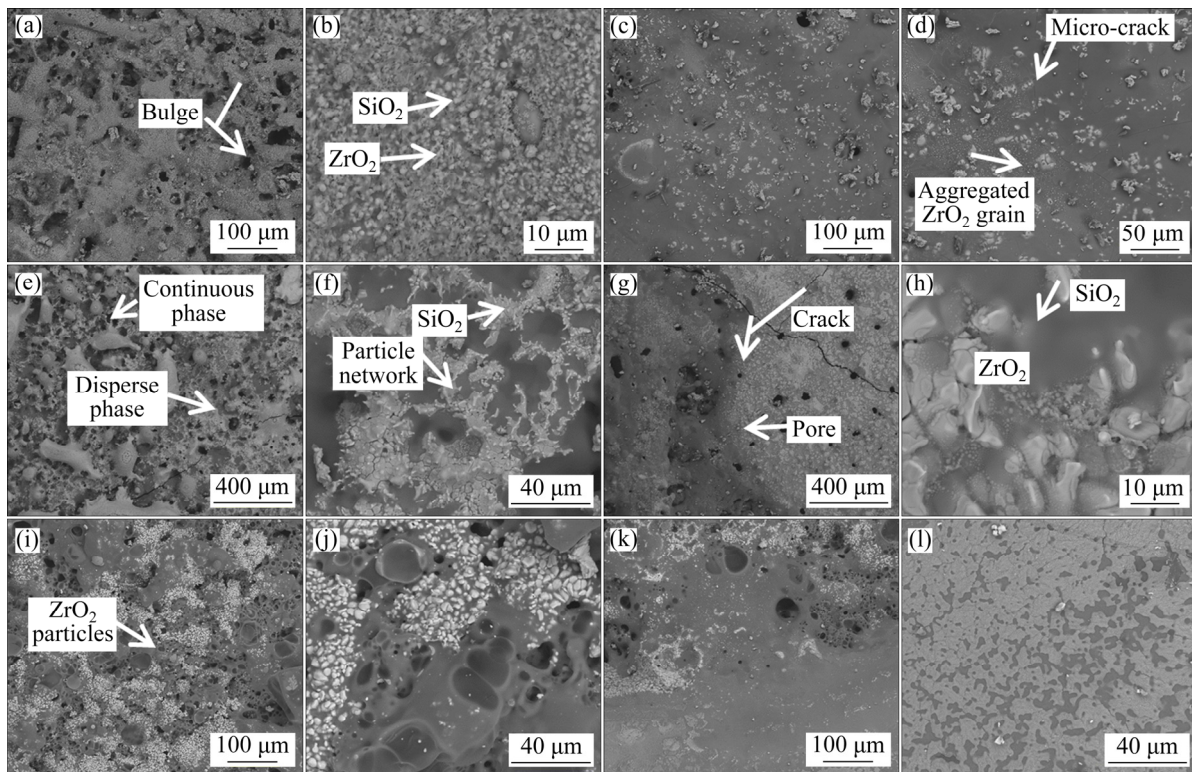
Fig. 6 Surface morphologies and EDX analysis results of ZSM-L samples after ablation for 60 s: (a−d) Condition 1; (e−h) Condition 2; (i−l) Condition 3; (a, b, e, f, i, j) Central area; (c, d, g, h, k, l) Transition area

area, the glassy layer is continuous with a few micro-cracks. Under Condition 2 (Figs. 7(e−h)), the coating is composed of a dispersed phase and a continuous phase in the central area. The dispersed phase is formed by the aggregation of white particles, with a dendritic-like structure (Fig. 7(f)). In the transition area, the distribution of the dispersed phases and the continuous phase is more uniform, with some pores and cracks existing. Under Condition 3 (Figs. 7(i−l)), a relatively complete structure is formed in the central area, and agglomerated ZrO_2 grains are embedded in the porous liquid phase. In the transition area, the $ZrSiO_4$ phase is continuous and distributed uniformly with SiO_2, forming $ZrSiO_4$−SiO_2 double layer, which can provide oxidation and ablation protection for C/C−SiC−ZrC composites.

From the surface images of the ablated ZSM-L and ZSM-H samples, it can be seen that, with the increase of heat fluxes, the content of ZrO_2 and pores induced by the evaporation of gas products increases, while SiO_2 gradually depletes. Under Conditions 1 and 2, the ZrO_2 phase with smaller particle size has a stronger pinning effect on the glass phase SiO_2, resulting in a reduction of the depletion of liquid phase. So, fewer pores, higher flatness, and a more uniform distribution of SiO_2 and ZrO_2 are observed on the surface of ZSM-H samples. Hence, ZSM-H samples exhibit better performance than ZSM-L samples under Conditions 1 and 2. However, under Condition 3, ZSM-H samples have a higher linear ablation rate. This is mainly attributed to the low content of SiC in the coating and, therefore, lack of liquid phase to connect the loose ZrO_2 skeleton.

Figure 8 illustrates the backscattered electron (BSE) SEM images of the cross-section of ZSM-L and ZSM-H samples after ablation under three

Fig. 7 Surface morphologies of ZSM-H samples after ablation for 60 s: (a−d) Condition 1; (e−h) Condition 2; (i−l) Condition 3; (a, b, e, f, i, j) Central area; (c, d, g, h, k, l) Transition area

conditions. The coatings can be divided into two layers: the transition ZrO_2−SiO_2 layer (Layer 1) and the molten filled layer (Layer 2), which is mainly composed of ZrO_2, SiO_2, and molten-$ZrSiO_4$.
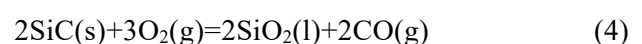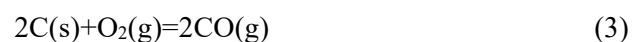
Under Condition 1 (Figs. 8(a, d)), fine ZrO_2 particles appear "rose-like" skeletons in the molten filled layer, in which gaps in the skeletons are sealed by SiO_2 glass. Under Condition 2 (Figs. 8(b, e)), a dense ZrO_2 scale is formed on the exterior layer, which is dense enough to block the infiltration of oxygen. Under Condition 3 (Figs. 8(c, f)), the transition layer is the thinnest under all conditions. ZrO_2 acts as a skeleton of the coating after ablation, which reduces the evaporation of SiO_2, so the mass proportion of Zr in the coating system is of great importance. In Condition 1 and Condition 2, ZSM-H sample can protect matrix better because smaller ZrO_2 particles provide stronger pinning effect. However, in Condition 3, ZSM-L sample has better performance by forming continuous liquid oxide layer.
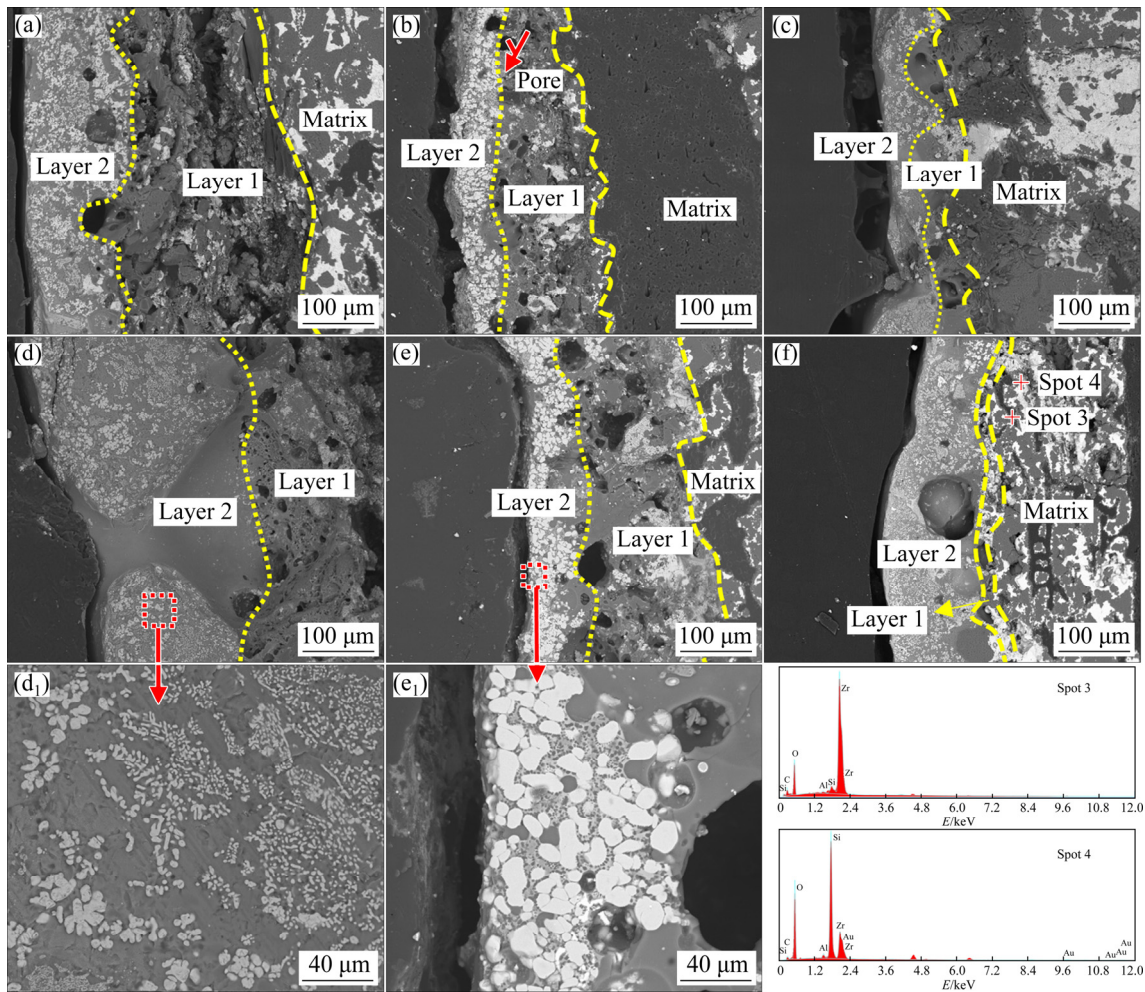
Both of the ZSM-L and ZSM-H coatings consist of ZrO_2 grains and liquid phases of SiO_2 and $ZrSiO_4$. Two layers with distinct structure can be detected in the cross-section images. The molten filled layer can effectively prevent the diffusion of oxygen into the inner coating and reduce the mechanical denudation caused by the high-speed gas fluxes. In addition, the transition ZrO_2−SiO_2 layer can further prevent oxygen from infiltrating into the substrate.
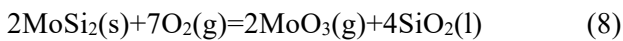
3.4 Ablation mechanisms

The schematic of the ablation process of the coatings under three conditions is illustrated in Fig. 9. The ablation mechanisms of ZSM coatings are accompanied by a series of chemical erosion and mechanical denudation. Chemical erosion is mainly attributed to the reactions between ZSM coatings and oxygen. Mechanical denudation includes the release of volatile gas (CO_2, CO, MoO_3, SiO_2, SiO), as well as peeling, cracking and melting caused by high-temperature, high-pressure gas flow [27]. During the ablation test, the main possible reactions are as follows:

$$C(s)+O_2(g)=CO_2(g) \tag{2}$$

$$2C(s)+O_2(g)=2CO(g) \tag{3}$$

$$2SiC(s)+3O_2(g)=2SiO_2(l)+2CO(g) \tag{4}$$

$$SiC(s)+O_2(g)=SiO(g)+CO(g) \tag{5}$$

Fig. 8 BSE SEM images and EDX analysis results of cross-section of ZSM coatings after ablation: (a−c) ZSM-L sample; (d−f) ZSM-H sample; (a, d) Condition 1; (b, e) Condition 2; (c, f) Condition 3; (d$_1$): Enlarged view of (d); (e$_1$) Enlarged view of (e)

$$SiC(s)=SiC(l)=SiC(g) \tag{6}$$

$$2ZrC(s)+3O_2(g)=2ZrO_2+2CO(g) \tag{7}$$

$$2MoSi_2(s)+7O_2(g)=2MoO_3(g)+4SiO_2(l) \tag{8}$$

The ablation behavior of ZSM coatings can be divided into three stages. In initial stage, ZrC, SiC, and MoSi$_2$ are oxidized to form ZrO$_2$ particles (Eq. (7)), liquid SiO$_2$ (Eq. (4)) and MoO$_3$ gas (Eq. (8)), respectively. In this stage, the coating protects the substrate through consuming a large amount of oxygen. Therefore, the ablation rate is mainly controlled by the oxidation rate of ZrC and SiC. In the middle stage, SiO$_2$ reacts with ZrO$_2$ to form molten ZrSiO$_4$. The molten ZrSiO$_4$ and SiO$_2$ can fill in the porous ZrO$_2$ skeleton and considerably reduce the number of pores. In this stage, the generating rate of liquid phase is higher than the removing rate which is caused by

evaporating and blowing away by high-speed gas flow. Therefore, the ablation rate in the middle stage is mainly controlled by the diffusion rate of oxygen through the oxide layer. In the final stage, lots of pores are formed in the oxide layer as the evaporation of SiO$_2$ increases, leaving a loose ZrO$_2$ skeleton on the coating surface. In this stage, the evaporating rate of liquid phase is higher than the filling rate of liquid phase in defects. Hence, the ablation rate is controlled by the diffusion rate of oxygen in the inner material.

In summary, the ablation behavior of the coatings varies with different ablation conditions. Taking the ZSM-H as a sample: under Condition 1, oxidation is the main mechanism of ablation, and no obvious denudation appears on the surface of the coatings. Moreover, a mosaic structure is formed by the liquid phase and ZrO$_2$ particles.
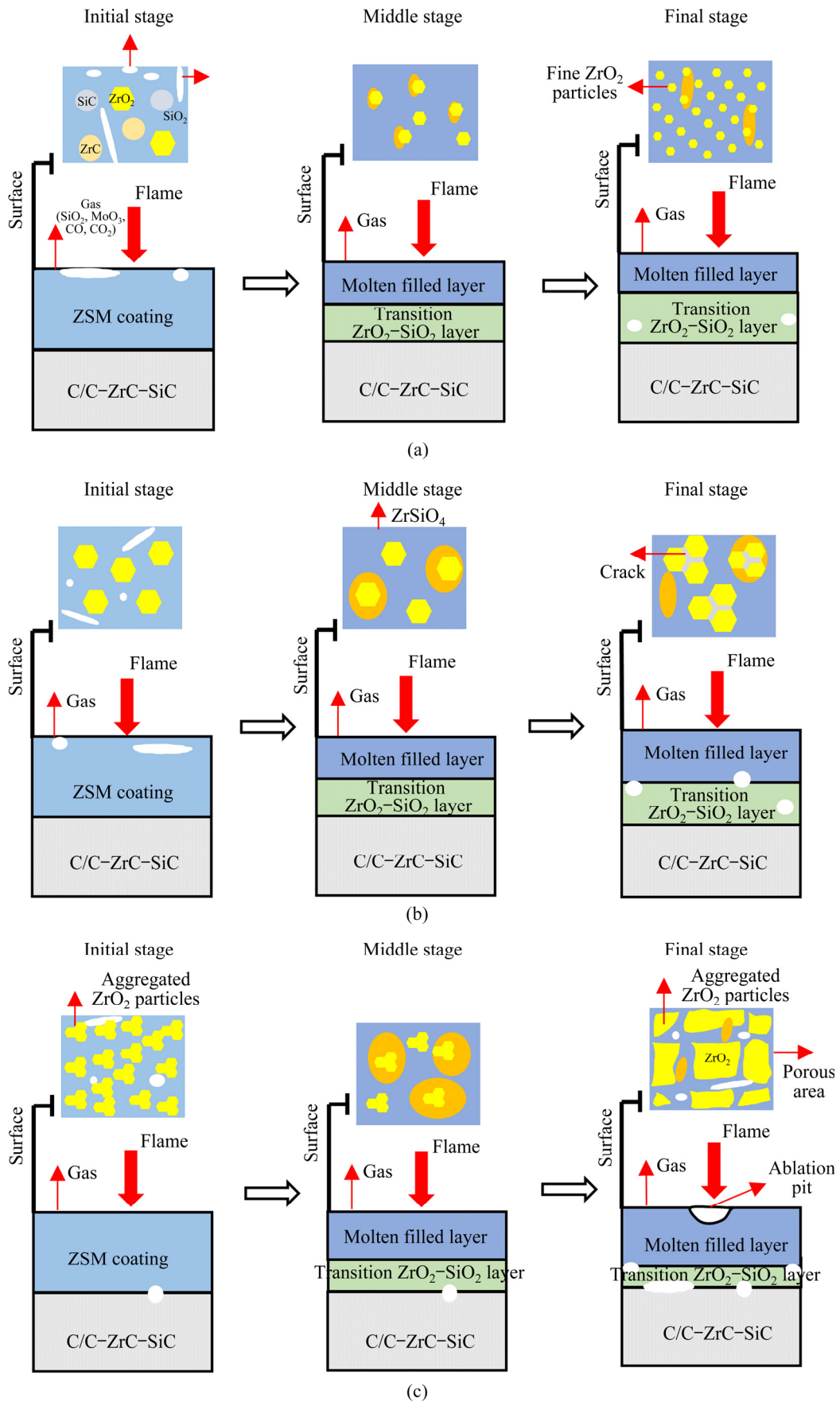
Fig. 9 Schematic of ablation mechanisms of ZSM coatings: (a) Condition 1; (b) Condition 2; (c) Condition 3

Under Condition 2, pores increase rapidly, and ZrO_2 grains aggregate. The main ablation mechanisms are oxidation associated with evaporation. Finally, under Condition 3, the formation of ablation pit is attributed to the denudation of gas flow. The ablation mechanisms are the combination of oxidation, evaporation and denudation.

4 Conclusions

(1) When the gas flows of O_2 and C_2H_2 were 1.1000, 0.2627 L/s and 1.5120, 1.1160 L/s, respectively, ZSM-H samples exhibit lower linear ablation rates than ZSM-L samples. When the gas flows of O_2 and C_2H_2 were increased to 2.000 and 1.1160 L/s, respectively, ZSM-L samples show a lower linear ablation rate.

(2) With the increase of heat fluxes, the morphology and structure of coatings change significantly. More SiO_2 glass phases with few pores and cracks exist under Condition 1; Aggregated big ZrO_2 particles with lots of cracks and pores are observed under Condition 2; More aggregated ZrO_2 particles but less SiO_2 phase form a porous area under Condition 3.

(3) The ablation behavior is controlled by the ablation of carbide in the initial stage, the diffusion of oxygen into the oxidized layer and through the defects in the middle and final stages, respectively.

(4) The main ablation mechanisms under Conditions 1, 2 and 3 are oxidation, oxidation plus evaporation, as well as a combination of oxidation, evaporation and denudation, respectively.

Acknowledgments

References

[1]   LI Bo, LI He-jun, YAO Xi-yuan, CHEN Yi-gao, HU Xu, FENG Guang-hui, LU Jin-hua. Ablation behavior of sharp leading edge parts made of rare earth La-compound modified ZrB_2 coated C/C composites [J]. Corrosion Science, 2020, 175: 108895.

[2]   RAN Li-ping, RAO Fei, PENG Ke, YIN Huan, YI Mao-zhong. Preparation and properties of C/C−ZrB_2−SiC composites by high-solid-loading slurry impregnation and polymer infiltration and pyrolysis (PIP) [J]. Transactions of Nonferrous Metals Society of China, 2019, 29(10): 2141−2150.

[3]   WANG Pei-pei, LI He-jun, YUAN Rui-mei, KONG Jing'an, LI Tao, ZHANG Yu-lei. A $CrSi_2$−HfB_2−SiC coating providing oxidation and ablation protection over 1973 K for SiC coated C/C composites [J]. Corrosion Science, 2020, 167: 108536.

[4]   HUO Cai-xia, ZHOU Lei, GUO Ling-jun, WANG Jian-cheng, LI Yun-yu, SUN Jia, LIU Lei. Effect of the Al_2O_3 additive on the high temperature ablation behavior of the ZrC−ZrO_2 coating for SiC-coated carbon/carbon composites [J]. Ceramics International, 2019, 45(17): 23180−23195.

[5]   XU Xue-ting, PAN Xiao-hui, NIU Ya-ran, LI Hong, NI De-wei, HUANG Shang-song, ZHONG Xin, ZHENG Xue-bin, SUN Jin-liang. Difference evaluation on ablation behaviors of ZrC-based and ZrB_2-based UHTCs coatings [J]. Corrosion Science, 2021, 180: 109181.

[6]   LI Jun, YANG Xin, SU Zhe-an, XUE Liang, ZHONG Ping, LI Shuai-peng, HUANG Qi-zhong, LIU Hong-wei. Effect of ZrC−SiC content on microstructure and ablation properties of C/C composites [J]. Transactions of Nonferrous Metals Society of China, 2016, 26(10): 2653−2664.

[7]   LI Yang, XIAO Peng, LI Zhuan, LUO Wei, ZHOU Wei. Oxidation behavior of C/C composites with $SiC/ZrSiO_4$−SiO_2 coating [J]. Transactions of Nonferrous Metals Society of China, 2017, 27(2): 397−405.

[8]   HE Qin-chuan, LI He-jun, YIN Xue-min, LU Jin-hua. Effects of PyC shell thickness on the microstructure, ablation resistance of SiCnws/PyC−C/C−ZrC−SiC composites [J]. Journal of Materials Science & Technology, 2021, 71: 55−66.

[9]   LI Qing-gang, DONG Shao-ming, WANG Zhi, HUANG Shi-feng, CHENG Xin. Ablation behavior and mechanism of 3D Cf/ZrC−SiC composites in a plasma wind tunnel environment [J]. Journal of Asian Ceramic Societies, 2018, 3(4): 377−382.

[10]   XIE Jing, JIA Yu-jun, ZHAO Zhi-gang, LI Ke-zhi, SUN Guo-dong, LI Hui, SU Xing-hua. A ZrC SiC/SiC multilayer anti-ablation coating for ZrC modified C/C composites [J]. Vacuum, 2018, 157: 324−331.

[11]   ZHANG Jian, ZHANG Yu-lei, FU Yan-qin, HU Du, MENG Jia-chen, LI Tao. Ablation behavior of HfC coating with different thickness for carbon/carbon composites at ultra-high temperature [J]. Journal of the European Ceramic Society, 2021, 41(3): 1769−1778.

[12]   PAN Xiao-hui, LI Chong, NIU Ya-ran, ZHONG Xin, HUANG Li-ping, ZENG Yi, ZHENG Xue-bin. Effect of Yb_2O_3 addition on oxidation/ablation behaviors of ZrB_2−$MoSi_2$ composite coating under different environment [J]. Corrosion Science, 2020, 175: 108882.

[13]   XU Jun-jie, SUN Wei, XIONG Xiang, XU Yong-long, DENG Nan-jun, LI Wan-qian, CHEN Zhao-ke. Micro-structure and ablation behaviour of a strong, dense, and thick interfacial $Zr_xHf_{1-x}C$/SiC multiphase bilayer coating prepared by a new simple one-step method [J]. Ceramics International, 2020, 46(8): 12031−12043.

[14] ZHANG Pei, FU Qian-gang, CHENG Chun-yu, ZHU Xiao-fei, HUANG Jin-guo, ZHANG Jia-ping, LI Wei. Comparing oxidation behaviors at 1773 K and 1973 K of HfB₂−MoSi₂/SiC−Si coating prepared by a combination method of pack cementation, slurry painting and in-situ synthesis [J]. Surface and Coatings Technology, 2020, 403: 126418.

[15] QIAN Tian-xiao, ZENG Yi, XIONG Xiang, YE Zi-ming, LUN Hui-lin, HU Jin-run, WANG Ya-lei, ZHANG Zhong-wei, YAN Chang-hai. Corrosion behavior of Y₂O₃-doped mullite-ZrSiO₄ coatings applied on C/C−SiC composites in the presence of moisture at temperatures of 1373−1773 K [J]. Ceramics International, 2020, 46(8): 12861−12869.

[16] HUO Cai-xia, GUO Ling-jun, ZHOU Lei, LIU Bing, WANG Chang-cong, ZHANG Yu-lei, WANG Hai-qi. Effect of Al₂O₃ addition on the ablation behavior of SiC−ZrC coated C/C composites [J]. Journal of Alloys and Compounds, 2018, 752: 489−504.

[17] LIU Tao, NIU Ya-ran, LI Chong, PAN Xiao-hui, SHI Min-hao, ZHENG Xue-bin, DING Chuan-xian. Ablation resistance of ZrC−MoSi₂/ZrC−SiC double-layered coating in a plasma flame [J]. Corrosion Science, 2018, 145: 239−248.

[18] JIANG Yan, LIU Tian-yu, RU Hong-qiang, WANG Wei, ZHANG Cui-ping, YUE Xin-yan. Oxidation and ablation protection of double layer HfB₂−SiC−Si/SiC−Si coating for graphite materials [J]. Journal of Alloys and Compounds, 2019, 782: 761−771.

[19] WANG Shao-long, LI Ke-zhi, LI He-jun, ZHANG Yu-lei, ZHANG Wei-yang. Ablation behavior of CVD-ZrC coating under oxyacetylene torch environment with different heat fluxes [J]. International Journal of Refractory Metals and Hard Materials, 2015, 48: 108−114.

[20] HAO Jian-jie, LI Jia-yan, SHI Wei, WANG Bo, TAN Yi. The novel effect mechanism of Al₂O₃ nano-powder in the pack cementation process to prepare SiC coating on C/C composites [J]. Journal of the European Ceramic Society, 2021, 41(2): 1107−1113.

[21] PENG Zheng, SUN Wei, XIONG Xiang, XU Yong-long, CHEN Yun-tian. A novel Cr-doped Al₂O₃−SiC−ZrC composite coating for ablative protection of C/C−ZrC−SiC composites [J]. Journal of the European Ceramic Society, 2018, 38(7): 2897−2902.

[22] LIANG Han-qin, YAO Xiu-min, ZHANG Jing-xian, LIU Xue-jian, HUANG Zheng-ren. Low temperature pressureless sintering of α-SiC with Al₂O₃ and CeO₂ as additives [J]. Journal of the European Ceramic Society, 2014, 34(3): 831−835.

[23] WANG Jun-xia, YANG Ke-ming, WANG Jin, YANG Shi-yuan, ZHANG Xiu-lu. The enhanced structure stability and the reinforcement mechanism of 0.1Al₂O₃−ZrO₂ reinforced MoSi₂ composite coating [J]. Surface and Coatings Technology, 2020, 403: 126438.

[24] LI Jin-hua, ZHANG Yu-lei, WANG Hao-hao, FU Yan-qin, CHEN Guo-hui, XI Zeng-zhe. Long-life ablation resistance ZrB₂−SiC−TiSi₂ ceramic coating for SiC coated C/C composites under oxidizing environments up to 2200 K [J]. Journal of Alloys and Compounds, 2020, 824: 153934.

[25] PAN Xiao-hui, NIU Ya-ran, XU Xue-ting, ZHONG Xin, SHI Min-hao, ZHENG Xue-bin, DING Chuan-xian. Long time ablation behaviors of designed ZrC−SiC−TiC ternary coatings for environments above 2000 °C [J]. Corrosion Science, 2020, 170: 108645.

[26] YANG Xiao-ting, QUAN Hua-feng, WANG Ke. SiC/Si−ZrSi₂−ZrB₂−HfB₂/SiC coating for oxidation protection of C/C composites prepared by three-step method [J]. Journal of Alloys and Compounds, 2020, 836: 155532.

[27] LIU Tao, NIU Ya-ran, LI Chong, ZHAO Jun, ZHANG Ji-mei, ZENG Yi, ZHENG Xue-bin, DING Chuan-xian. Effect of MoSi₂ addition on ablation behavior of ZrC coating fabricated by vacuum plasma spray [J]. Ceramics International, 2018, 44 (8): 8946−8954.

ZrC−SiC−MoSi₂ 涂覆 C/C−SiC−ZrC 陶瓷基复合材料在氧乙炔焰下的烧蚀行为及机理

邵萌萌，陈招科，王馨爽，文青波，熊 翔

中南大学 粉末冶金国家重点实验室，长沙 410083

摘　要：为进一步提高 C/C 复合材料在不同烧蚀环境下的烧蚀性能，采用浆料刷涂法在 C/C−SiC−ZrC 陶瓷基复合材料上制备 Zr 含量分别为 34%和 60%(质量分数)的 ZrC−SiC−MoSi₂ 涂层，并且利用氧乙炔焰研究涂层 C/C−SiC−ZrC 复合材料在 3 种不同氧气及乙炔流量下的烧蚀行为。结果表明：随着 Zr 含量的增加，涂层内部的 ZrC 和 SiC 颗粒尺寸明显减小，且颗粒分布更加均匀。Zr 含量为 60%的涂层线烧蚀率随氧气和乙炔流量的增加而增加，而 Zr 含量为 34%的涂层线烧蚀率随氧气和乙炔流量的增加，先增加后降低。此外，详细讨论 ZrC−SiC−MoSi₂ 涂层在不同条件下的烧蚀机理。随着氧气和乙炔流量的增加，主要的烧蚀机制由氧化变为氧化和蒸发的结合作用，最后变为氧化、蒸发及剥蚀的结合作用。

关键词：C/C−SiC−ZrC 复合材料；ZrC−SiC−MoSi₂ 涂层；刷涂；烧蚀

(Edited by Bing YANG)